Harnessing intrinsic electric fields in 2D Janus MoOX (X=S, Se, and Te) monolayers for enhanced photocatalytic hydrogen evolution

Haman, Zakaryae; Kibbou, Moussa; Khossossi, Nabil; Ouabida, Elhoussaine; Dey, Poulumi; Essaoudi, Ismail; Ainane, Abdelmajid

DOI
10.1016/j.ijhydene.2024.04.257

Publication date
2024

Document Version
Final published version

Published in
International Journal of Hydrogen Energy

International Journal of Hydrogen Energy 68 (2024) 566–574

Contents lists available at ScienceDirect

International Journal of Hydrogen Energy

journal homepage: www.elsevier.com/locate/he

Harnessing intrinsic electric fields in 2D Janus MoOX (X=S, Se, and Te) monolayers for enhanced photocatalytic hydrogen evolution

Zakaryae Haman [a,*], Moussa Kibbou [a], Nabil Khossossi [b,*], Elhoussaine Ouabida [c], Poulumi Dey [b], Ismail Essaoudi [a], Abdelmajid Ainane [a,*]

[a] Laboratoire de Physique des Matèriaux et Modélisations des Systèmes, (LP2MS), Faculty of Sciences, Department of Physics, Moulay Ismail University, Meknes, Morocco

[b] Department of Materials Science and Engineering, Faculty of Mechanical Engineering, Delft University of Technology, Mekelweg 2, Delft, 2628 CD, The Netherlands

[c] Advanced Systems Engineering Laboratory, National School of Applied Sciences, Ibn Tofail University, University Campus, Po Box 242, Kenitra, Morocco

ARTICLE INFO

Keywords:
2D janus monolayer
Optical absorption
Hydrogen evolution reaction
Solar to hydrogen efficiency
First-principles calculations

ABSTRACT

Two-dimensional (2D) Janus monolayers, distinguished by their intrinsic vertical electric fields, emerge as highly efficient and eco-friendly materials for advancing the field of hydrogen evolution reactions (HER). In this study, we explore, for the first time, the potential viability of the oxygenation phase of two-dimensional Janus transition metal dichalcogenides MoOX (X = S, Se, and Te) monolayers as an exceptionally efficient photocatalyst for hydrogen production. Based on first-principles computations, we demonstrate that all three monolayers exhibit semiconductor behavior, characterized by a band gap ranging from 0.66 to 1.55 eV. This narrow band gap renders the proposed materials highly efficient at absorbing light within the visible region. Excitingly, the introduction of an electrostatic potential difference $\Delta\Phi$ has granted us the ability to surpass the conventional bandgap limit ($E_g \geq 1.23$). Consequently, all monolayers exhibit favorable band alignment with respect to the vacuum level. Moreover, the calculated solar-to-hydrogen efficiency for the envisaged monolayer exceeds the established theoretical limit. Particularly, the MoOTe monolayer emerges as an infrared-light-driven photocatalyst, demonstrating a remarkable solar-to-hydrogen efficiency limit of up to 25,21% when considering the entire solar spectrum. A thorough examination of the Gibbs free energy differences across these monolayers has revealed that the values during the oxygenation phase are significantly smaller and approach the optimum, in contrast to the parental two-dimensional Janus transition metal dichalcogenides. Our results conclusively establish that the proposed materials exhibit exceptional efficiency as photocatalysts for hydrogen evolution reactions. Notably, their efficacy is demonstrated even in the lack of co-catalysts or sacrificial agents.

1. Introduction

In light of the increasing energy demand and the need to reduce emissions, the conversion of renewable and environmentally friendly fuels from infinite solar energy is regarded as an optimal approach to address the shortage of energy [1–4]. In this regard, photocatalytic water splitting has piqued interest as one of the prospective solutions for directly converting solar energy into hydrogen fuel in the face of the impending energy and environmental crises [5–7]. The relevance of hydrogen as a fuel stems from the high yield of energy emitted during burning, which much outperforms that of gasoline or any other kind of fossil fuel [8–11]. To enable the practical implementation of photocatalytic water-splitting in industrial settings, a key hurdle to address pertains to the evolution of photocatalysts that possess a considerable degree of efficiency in converting solar energy to hydrogen (STH) [12,13]. The improvement of the solar-to-hydrogen efficiency of photocatalysts is primarily hindered by three key challenges. Firstly, to achieve compatibility with the hydrogen reduction potential of H^+/H_2 (approximately 4.44 eV) and the water oxidation potential of H_2O/O_2 (around 5.67 eV), the photocatalyst's band gap must exceed 1.23 eV. Hence, catalysts with larger band gaps (greater than 3 eV) are incapable of absorbing photons with longer wavelengths, leading to a notable decrease in the performance of harnessing infrared light [14–17]. Secondly, the holes and electrons created by light in these photocatalysts must have the capability to quickly separate and move to prevent

* Corresponding authors.
E-mail addresses: zakaryae.haman@edu.umi.ac.ma (Z. Haman), n.khossossi@tudelft.nl (N. Khossossi), a.ainane@fs-umi.ac.ma (A. Ainane).

https://doi.org/10.1016/j.ijhydene.2024.04.257
Received 30 January 2024; Received in revised form 2 April 2024; Accepted 22 April 2024
Available online 30 April 2024

them from recombining, else the efficiency of the solar-to-hydrogen (STH) conversion will be significantly decreased [18]. Experimental studies have established that the mechanism of photocatalysis can be significantly increased, approximately by a factor of ninety, through the promotion of carrier separation [19,20]. Thirdly, both the conduction band minimum (CBM) and valence band maximum (VBM) of the photocatalysts should align in a suitable manner with the energy levels associated with the oxygen evolution reaction (OER) and hydrogen evolution reaction (HER) [21,22]. In addition, the HER and OER frequently require the application of overpotential, leading to a reduction in overall efficiency. Under ideal circumstances, characterized by optimal light absorption and carrier separation, and at the pinnacle of quantum efficiencies, the theoretical maximal efficiency can approximate 47% [23]. When taking into account the combined effects of further heat losses and other interconnected factors, the STH system can only achieve an efficiency of 18% [24]. In order to overcome the aforementioned constraints, a novel process of photocatalytic water splitting has arisen in two-dimensional (2D) materials [25]. The insertion of the intrinsic out-of-plane electric field was intended to affect the alignment of the CBM and VBM of the photocatalysts in relation to the potential for water reduction and oxidation. The bandgap limitation of typical photocatalysts (1.23 eV) is not only overcome but also enhanced redox capabilities are maintained to facilitate the HER and OER processes [26–30]. The inherent electric field additionally facilitates the acceleration and dispersion of the photogenerated holes and electrons. Within this particular framework, several 2D materials with a natural electric field perpendicular to their surface have been suggested as photocatalysts for water splitting [31,32]. Specifically, it has been predicted that $III_2 - VI_3$ materials, can achieve high solar-to-hydrogen (STH) efficiencies owing to the substantial contribution of the intrinsic electric field in the mechanism of photo-catalytic water splitting [33–35]. It is worth mentioning that Janus structures, an emerging category of two-dimensional (2D) materials, have garnered growing interest among scientists in recent times on account of their inherent out-of-plane polarization and fractured mirror symmetry. Janus MoSSe monolayer was effectively synthesized in 2017 through chemical vapor deposition (CVD) technique, employing two distinct approaches: selenization of MoS2 monolayer10 and sulfurization of MoSe2 monolayer. The effective synthesis of MoSe has generated considerable interest in the pursuit of analogous Janus monolayers exhibiting distinctive characteristics lacking in conventional two-dimensional materials. For example, the inherent out-of-plane mirror asymmetry of Janus monolayers has been postulated to enable them to function as effective photocatalysts for water splitting applications [36,37]. Inspired by these groundbreaking advancements, much research has been conducted on a range of Janus structures possessing inherent dipoles. For example, Ju et al. conducted a thorough examination of the significant characteristics of WSSe in relation to water splitting [38]. These characteristics include exciton binding energy, carrier mobility, and STH conversion efficiency, all of which are strongly linked to the performance of photocatalysis. The results indicate that Janus WSSe has superior photocatalytic performance compared to its parent materials (WS_2 and WSe_2). Further investigation has been devoted to the oxygenation process of Janus monolayers in two dimensions [39]. It is anticipated that oxygen's interaction with two-dimensional materials will significantly alter their physical properties [40]. The oxygenation of two-dimensional Janus transition metal dichalcogenide monolayers MoOX (X = S, Se, and Te) has been constructed and analyzed using DFT simulations.[41]. These materials have shown promising potential for application in photocatalytic water splitting, but an in-depth understanding is still lacking. Herein, inspired by the intriguing characteristics of two-dimensional Janus structures, we have thoroughly examined the photo-catalytic efficiency and underlying mechanism of the two-dimensional Janus transition metal oxides in the process of hydrogen evolution reaction. Our Results show that the oxygenation phase of two-dimensional Janus transition metal dichalcogenides (JTMDs) stands out prominently for its exceptional and superior properties. Notably, the solar-to-hydrogen efficiency attains an impressive 25.21% for molybdenum oxytelluride (MoOTe), surpassing the performance of all conventional two-dimensional JTMDs. This remarkable achievement underscores the promising potential of oxygenated JTMDs in advancing the field of solar energy conversion, particularly from the perspective of hydrogen production.

2. Computational methods:

VASP (Vienna-Ab Initio-Simulation-Package) was used to carry out our first-principles calculations, which were based on the density functional theory (DFT) [42,43]. The Perdew–Burke–Ernzerhof (PBE) generalized gradient approximation (GGA) was used to perform structural relaxation and static self-consistent computations. This approximation accounts for the exchange–correlation energy [44]. The electrical properties were determined accurately using the Heyd–Scuseria–Ernzerhof hybrid functional (HSE-06) with $\alpha = 0.25$ of Hartree–Fock exchange energy [45]. This specific choice has been demonstrated to effectively validate the experimental band gaps of semiconductors. The interaction between ions and electrons was simulated by employing projector-augmented wave potentials (PAWs), where semi-core electrons were considered as valence states [46]. To achieve a high level of accuracy in energy calculations, a cutoff energy of 500 eV was established to ensure precision within 10^{-5} eV/Å. For PBE calculations, Monkhorst–Pack k meshes with dimensions of $11 \times 11 \times 1$ were used. For HSE-06 calculations, Monkhorst–Pack k meshes with dimensions of $9 \times 9 \times 1$ were used [47]. Due to the asymmetrical feature of the Janus MoOS, MoOSe, and MoOTe monolayers, dipole correction was applied in all calculations. To reduce interlayer interactions, a vacuum space of around 20 Å was created along the Z direction. The Grimme dispersion correction DFT-D3 method was employed to account for the existence of weak van der Waals (vdW) interactions among interlayers [48,49]. To achieve accurate results in the complex dielectric functions related to optical absorption, a dense K-mesh was employed. The manuscript is further enriched with comprehensive details on Solar to hydrogen efficiency (STH) and on Gibbs free energy difference (ΔG_{H^*}) pertinent to HER. These details participate in the thoroughness and depth of the study.

3. Results and discussion:

3.1. Structural properties:

The crystal lattice of 2D JTMds with the formula MXY is notably derived from the parental 2D TMDs with the formula MX_2. The transformation from MX_2 to MXY introduces an intriguing asymmetry in the structural configuration, distinguishing Janus monolayers from their precursor materials. The selective engineering of this Janus structure holds great significance in tailoring the electronic and optical properties of these materials, as it provides unique opportunities for developing new photocatalysts for HER. The Janus MoOX monolayer is generated through the substitution of one layer of chalcogen atoms with oxygen atoms.

It is noteworthy that previous theoretical studies have consistently highlighted the high thermal and dynamical stability of all 2D MoOX monolayers. This indicates that these materials are capable of maintaining their structural integrity and performance across a wide range of temperatures and dynamic environments. As a result, the confirmed stability supports the feasibility of experimental synthesis and emphasizes the practical potential of these materials for real-world applications [50,51]. According to Fig. 1, the Janus MoOX monolayer maintains a hexagonal lattice similar to its parental phase. However, the introduction of oxygen (O) and another chalcogen element (X) causes a difference in atomic sizes, breaking the original symmetry of TMDs structure. This difference results in varying bond lengths for $Mo-O$ and $Mo-X$, emphasizing the unique structural features of the

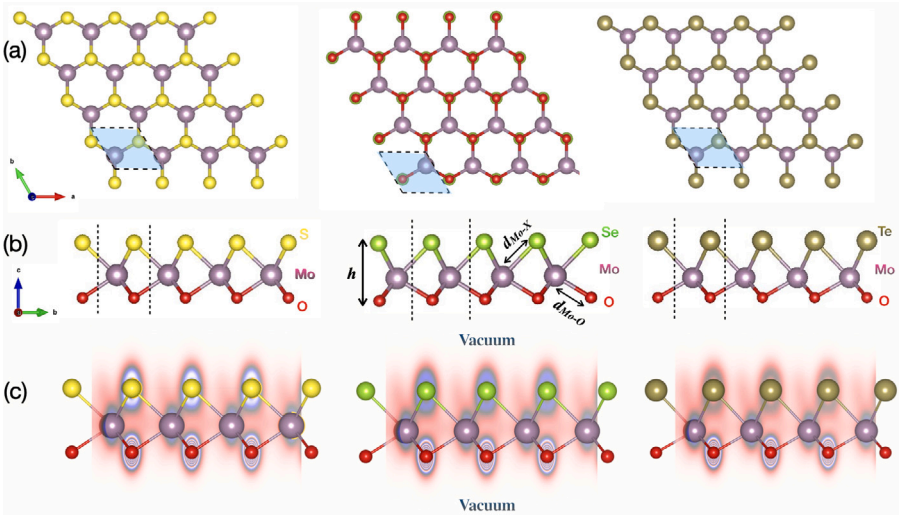

Fig. 1. (a) and (b) - Top and side views of the optimized 2D Janus MoOX monolayer. (c) - Side snapshot of the computed electron charge density. The dashed lines depict the unit cell.

Table 1
Computed lattice parameter (a), bond lengths (d), Band gap E_g and the electrostatic potential difference $\Delta\ \Phi$ for the three structures.

	a(Å)	d_{Mo-O} (Å)	d_{Mo-X} (Å)	h(Å)	E_g(HSE06)	$\Delta\ \Phi$
MoOS	3.009	2.088	2.382	2.788	1.563	2.29
MoOS	3.076	2.099	2.508	2.889	1.329	2.9
MoOTe	3.203	2.126	2.702	3.017	0.649	3.24

Table 2
The Bader charge transfer Q (|e|) between Mo, O and X in MoOX (X= S, Se and Te) monolayers.

Materials	$Q_{Mo}\|e\|$	$Q_O\|e\|$	$Q_S\|e\|$	$Q_{Se}\|e\|$	$Q_{Te}\|e\|$
MoOS	+2,0345	−1,1885	−0,846	–	–
MoOSe	+1,8678	−1,2005	–	−0,6673	–
MoOTe	+1,6281	−1,2097	–	–	−0,4185

Janus MoOX monolayer. Table 1 presents a comprehensive summary of the computed structural parameters. The bond length between Mo and X (d_{Mo-X}) shows an increase as the transition progresses from S to Te. This pattern is reflected in the lattice constant (a), which is directly proportional to d_{Mo-X}.

3.2. Electronic properties and band alignments of 2D janus moox monolayers:

Based on the optimized structure of Janus MoOX monolayers, we proceeded to examine their electronic properties, specifically by computing the band gap energy using the PBE and HSE06 approaches. Fig. 2 displays the band structure (BS) associated with the projected band structure of the 2D Janus MoOX monolayers, indicating that these materials are indirect semiconductors with a band gap ranging from 0.649 to 1.563 eV, as determined by the HSE06 functional, and it aligns with findings from earlier studies.

In combination with the suitable band gap energy, efficient water splitting in the photocatalysis process also relies on the presence of well-matched valence and conduction band edges in the photocatalyst. The redox potential linked to water splitting is dependent on the pH level, as indicated by the equation, $E_{H^+/H_2} = -4.44 + pH \times 0.059$ eV for the standard reduction potential of H^+/H_2. Simultaneously, the oxidation potential for O_2/H_2O can be determined using the equation $E_{O_2/H_2O} = -5.67 + pH \times 0.059$ eV.

Consequently, at a pH of 0, the standard redox potentials for H^+/H_2 and O_2/H_2O are measured at −4.44 and −5.67 eV, respectively. Subsequently, at a neutral pH of 7, the standard redox potentials for H^+/H_2 and O_2/H_2O are recalibrated to −4.027 and −5.257 eV, respectively. It is crucial to recognize that Janus structures, due to the absence of vertical mirror symmetry, give rise to intrinsic electric dipoles through charge migration between the upper and lower surfaces, as elucidated in the previous discussion. As a result, the surface of 2D Janus structures exhibits an observable electrostatic potential difference $\Delta\Phi$, leading to distinct values for the reduction potential of H^+/H_2 and the oxidation potential of O_2/H_2O. Therefore, it is crucial to include a dipole adjustment for systems that display asymmetry. Thus, all further discussions in this study are based on simulation findings that consider the dipole correction.

Incorporating a deeper understanding of the charge transfer between the Mo, O, and X atoms through Bader charge analysis is crucial for elucidating the electronic properties of the Janus MOX monolayer. Notably, the X atomic layer exhibits a lower electronegativity compared to the O atomic layer due to the greater atomic number of X relative to the O atom. This difference in electronegativity influences the charge distribution within the Janus structure, resulting in intriguing charge transfer dynamics as depicted in Fig. 1-(c). By employing Bader charge analysis, we can precisely quantify the redistribution of electronic charge among the constituent atoms, shedding light on the mechanisms underlying the electronic properties of the Janus MOX monolayer (See Table 2). For instance, in the case of MoOS, the Bader charge analysis reveals that Mo acquires a charge of +2.0345|e|, while O atoms exhibit charges of −1.1885|e|, and S atoms display charges of −0.846|e|. Hence, a built-in electric field (EF) exists within the Janus layer (See Fig. 3). The value of the electrostatic potential difference $\Delta\Phi$ rises with an increasing atomic number difference between O and X atoms. As an illustration, the difference in potential ($\Delta\Phi$) is 2.29, 2.9, and 3.24 electron volts (eV) in Janus MoOS, MoOSe, and MoOTe monolayers.

This variation in $\Delta\Phi$ can lead to electronic band bending, which in turn affects the photocatalytic performance. Fig. 4 presents an exhaustive examination of the relative band edge positions of 2D Janus MoOX monolayers with respect to vacuum levels. This evaluation incorporates considerations of the redox potentials associated with hydrogen (H^+/H_2) and oxygen (O_2/H_2O) production under differing pH conditions, specifically pH = 0 and pH = 7. Evidently, the band edges of the 2D Janus MoOX monolayers exhibit well-matched alignments, effectively straddling the redox potentials of water for both pH = 0 and pH = 7 environments. This observation underscores the potential of 2D Janus

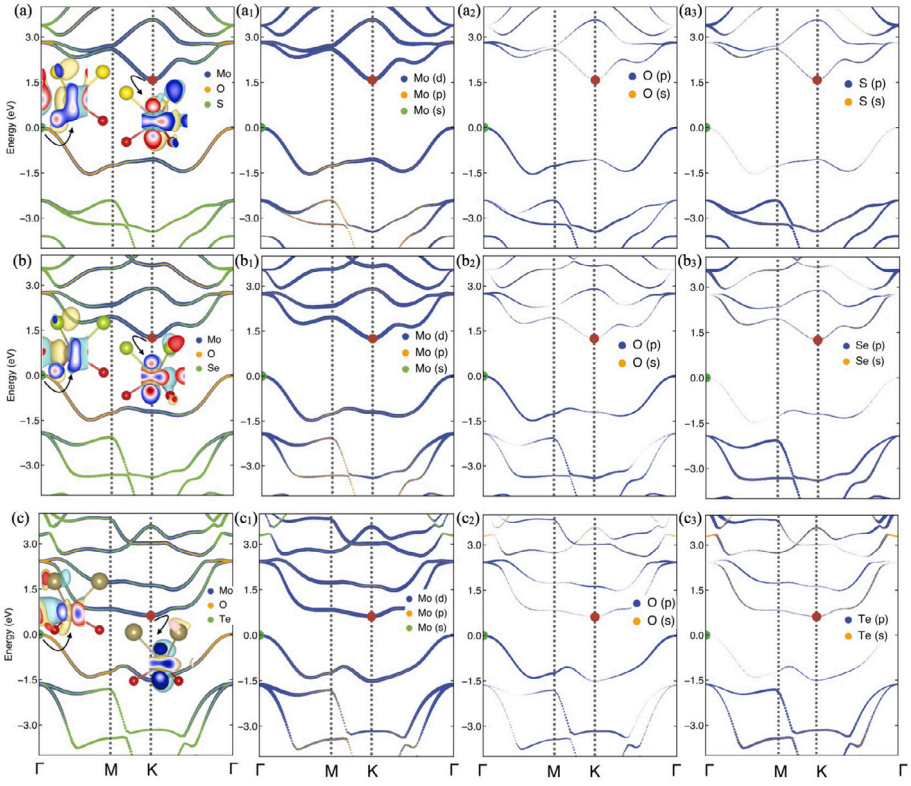

Fig. 2. Computed band structure and projected band structure of the 2D Janus MoOX monolayer utilizing the HSE06 functional.

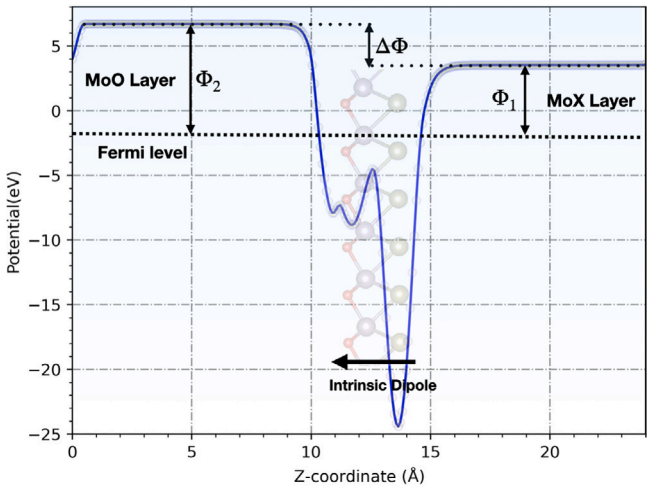

Fig. 3. Schematic representation of the electrostatic potential difference in 2D Janus MoOX monolayers along the *z*-axis direction.

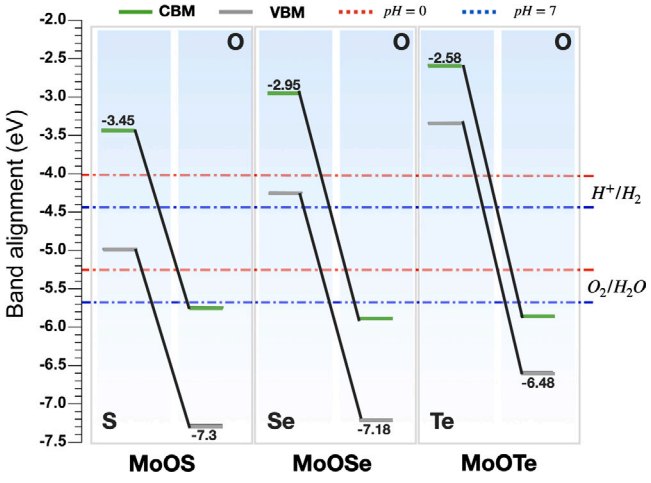

Fig. 4. Computed band edge positions for 2D Janus MoOX monolayers using the HSE06 functional. The blue and red dashed lines signify the redox potential of water at pH = 0 and pH = 7, respectively.

MoOX monolayers as promising photocatalysts for facilitating water splitting. Moreover, the overpotentials for HER denoted as $\chi(H_2)$ and Oxygen Evolution Reaction (OER) denoted as $\chi(O_2)$ serve as indicators of the redox capabilities of carriers generated through photocatalysis. These parameters are crucial benchmarks for assessing the efficiency of photocatalysts in the process of water splitting. Specifically, $\chi(H_2)$ is the potential difference between the CBM and the redox potential of H^+/H_2, while $\chi(O_2)$ represents the potential difference between the VBM and the redox potential of H_2O/O_2. The specific values for $\chi(H_2)$ and $\chi(O_2)$ can be found in Table 4. It is noteworthy that, without exception, all $\chi(H_2)$ and $\chi(O_2)$ values for the 2D Janus MoOX monolayers surpass 0.4 eV. This observation underscores the considerable redox capabilities exhibited by these materials in the context of HER and OER.

3.3. Optical absorption:

Due to the fact that the initial stage of photocatalysis involves the generation of electrons and holes through the use of photon absorption, the performance of optical response is of utmost importance. The optical properties of a material are elucidated by examining the frequency-dependent complex dielectric function, denoted as $\varepsilon(\omega) = \varepsilon_1(\omega) + i\varepsilon_2(\omega)$, as documented in existing literature [52–54].

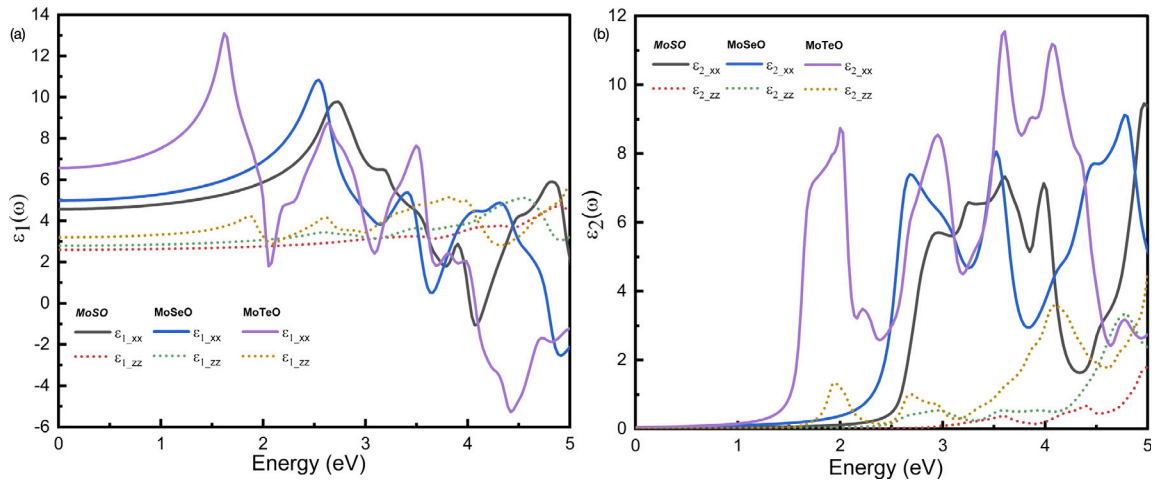

Fig. 5. Computed the real and the imaginary parts of the complex dielectric function for the 2D Janus MoOX monolayers using the HSE06 functional along the *xx* and *zz* directions.

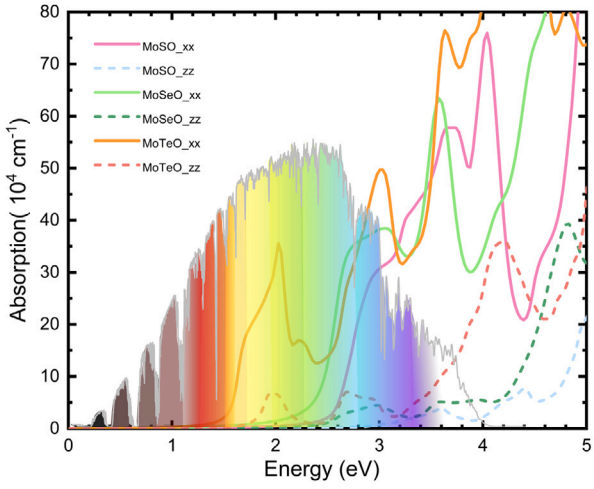

Fig. 6. Calculated Absorption coefficient for the 2D Janus MoOX monolayers using the HSE06 functional along the *xx* and *zz* directions.

The real part, $\varepsilon_1(\omega)$, is determined employing the Kramers–Kronig relation, while the imaginary part, $\varepsilon_2(\omega)$, is computed by aggregating contributions from unoccupied states across the Brillouin zone [55]. Subsequently, the absorption coefficient $\alpha(\omega)$ is ascertained using the prescribed equation. Fig. 5a displays the real component $\varepsilon_1(\omega)$ and Fig. 5 displays the imaginary part $\varepsilon_2(\omega)$ of the complex dielectric function for the two dimensional Janus transition metal oxides monolayers, respectively. The imaginary component $\varepsilon_2(\omega)$ exhibits several peaks, including a prominent peak at 1.5–3.5 eV, which is mostly attributed to the interband transition. The initial prominent peak of the imaginary component $\varepsilon_1(\omega)$ undergoes a downward shift in energy when X transitions from S to Te. This observation aligns with the corresponding variations in the band gaps. Based on the complex dielectric function, the absorption coefficient of our compounds is computed and depicted in Fig. 6. From Fig. 6, it is evident that the absorption spectra manifest a pronounced anisotropy, notably discernible along the X and Z directions. Moreover, the initial absorption peak transitions to lower energies as X changes from S to Te. This observation aligns with the fluctuating trends observed in the composition-dependent band gap. Visible light absorption coefficients are prominent in all monolayers, with MoOTe monolayer exhibiting a noteworthy absorption coefficient along the *zz*–direction, reaching up to 3.5×10^5 cm^{-1}. This highlights its efficient light harvesting in the visible region. The absorption coefficients of these materials are superior to those of 2D JTMDs or at least comparable to most known 2D absorber materials, this ensures that 2D Janus transition metal oxides monolayers are viable candidates for implementation in the domain of photocatalytic water splitting [56,57].

3.4. Hydrogen evolution reaction:

The Hydrogen Evolution Reaction performance of MoOS, MoOSe, and MoOTe monolayers is characterized by assessing the Gibbs free energy of the reaction intermediate (H^*), which is defined as [30]:

$$\Delta G_{H^*} = \Delta E_{H^*} + \Delta E_{ZPE} - T\Delta S, \tag{1}$$

The quantities ΔE_{ZPE} and $T\Delta S$ denote the entropy and change in zero-point energy, respectively, that occur during atomic hydrogen adsorption and hydrogen in the gas phase. The catalyst's contributions to both ΔE_{ZPE} and $T\Delta S$ are negligible, and can therefore be disregarded. Therefore, ΔE_{ZPE} can be calculated using the subsequent equation [58]:

$$\Delta E_{ZPE} = E_{ZPE}^{nH} - E_{ZPE}^{(n-1)H} - \frac{1}{2}E_{ZPE}^{\mathrm{H_2}}, \tag{2}$$

Where, E_{ZPE}^{nH} denotes the zero-point energy of n hydrogen atoms adsorbed on the monolayer without considering the catalyst's contribution, while $E_{ZPE}^{\mathrm{H_2}}$ denotes the zero-point energy of an H2 molecule in the gas phase. The quantity ΔE_{ZPE} is variable and ranges from −0.01 to 0.04 eV. The entropy of atomic hydrogen, ΔS_H (approximately $-\frac{1}{2}\Delta S_H^0$, where ΔS_H^0 signifies the entropy of an H_2 molecule in the gas phase. The value of TS_H^0 is considered as 0.4 eV at $T = 300$ K, resulting in $\Delta E_{ZPE} - T\Delta S$ equal to 0.24 eV [59]. Consequently, the adsorption-free energy pertinent to the HER mechanism can be regarded as:

$$\Delta G_{H^*} = E_{ads} + 0.24, \tag{3}$$

In the case of an ideal catalyst, ΔG_{H^*} ought to equal zero [59]. The hydrogen binding energy, denoted as E_{ads}, which is defined as:

$$E_{ads} = E_{monolayer+nH} + E_{monolayer+(n-1)H} - \frac{1}{2}E_{\mathrm{H_2}} \tag{4}$$

In this expression, $E_{monolayer+nH}$ and $E_{monolayer+(n-1)H}$ represent the total energy of the monolayer with n and n-1 adsorbed hydrogen atoms, respectively, and $E_{\mathrm{H_2}}$ is the total energy of H_2 molecules in the gas phase.

To initiate the practical photocatalytic processes of HER, the photogenerated carriers must supply a substantial driving force, specifically, a sufficient external potential. Otherwise, supplementary measures, such as the introduction of sacrificial reagents or cocatalysts, become

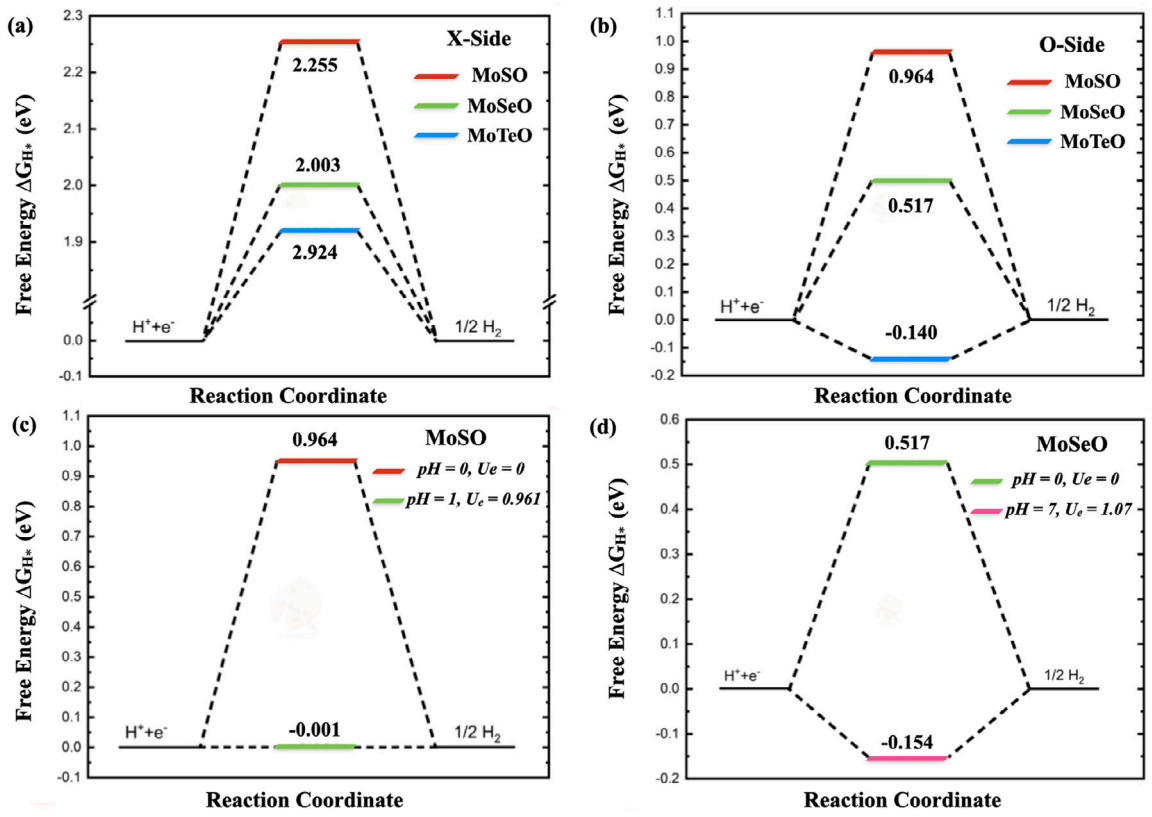

Fig. 7. (a) and (b) computed the Gibbs free energy difference for the 2D Janus MoOX monolayer on the X and O sides, respectively. (c) and (d) calculated the ΔG_{H^*} at different values of pH and U_e for MoOS and MoOSe, respectively.

necessary. The potential contribution of photogenerated electrons in photocatalysts for HER (U_e) was calculated using $U_e = CBM - (-4.44 + 0.059 \times pH)$ pertaining to previous investigations [60,61].

For MoOS, MoOSe, and MoOTe, under the standard hydrogen electrode at pH 0, their Ue values are 1.21, 0.99, and 1.86 eV, respectively. Consequently, all these structures exhibit substantial potentials conducive to hydrogen production via water splitting. The computed Gibbs free energy differences for the O and X sides of these three monolayers are illustrated in Fig. 7. Notably, the Gibbs free energy values on the O side are consistently smaller than those on the X side.

T he computed Gibbs free energy differences between the O and X sides of the three monolayers, as depicted in Fig. 7, reveal a consistent trend: the Gibbs free energy values on the O side consistently outweigh those on the X side. Particularly noteworthy is the comparison between the computed Gibbs free energy of 2D Janus MoOX and its parental MXY counterparts. Surprisingly, the Janus MoOX exhibits significantly inferior Gibbs free energy values compared to its predecessors, with respective values of 2.04, 2.17, and 2.29 eV for MoSSe, MoSeTe, MoSTe [27,62]. However, the difference in Gibbs free energy is closely linked to the strength of adsorbed energy, which is influenced by a multitude of factors. These include the band gap, surface morphology, lattice parameters, position of the conduction band minimum (CBM), and electrostatic interactions. The intricate interplay of these factors ultimately determines the stability and energetics of the monolayers, thus reflecting in the computed Gibbs free energy values [63].

For MoOS and MoOSe, the initial Gibbs free energy values are notably distant from the optimal condition. However, under pH = 1 and $U_e = 0.96$, the Gibbs free energy value for MoOS tends to −0.001, which is close to the ideal value. Similarly, under pH = 7, the external potential U_e for MoOSe is equal to 1.17, and the Gibbs free energy under these conditions is −0.15, which is near the ideal value (see Fig. 7).

Table 3
Summary of various photocatalytic properties of 2D MoOX monolayers, including the Over-Potential for HER ($\chi(H_2)$) and OER ($\chi(O_2)$), photon energy (E) at different $pH = 4$, as well as the efficiency of light absorption (η_{abs}), carrier utilization (η_{cu}), Solar-to-Hydrogen (STH) efficiency η_{STH}), and the corrected Solar-to-Hydrogen (STH) efficiency (η'_{STH}).

	$\chi(H_2)$	$\chi(O_2)$	E	η_{abs}	η_{cu}	η_{STH}	η'_{STH}
MoOS	0.403	0.177	2.233	58.01	56.6	32.84	20.38
MoOS	0.344	0.236	2.174	70.47	61.61	43,42	21.45
MoOTe	0.285	0.295	2.115	96	78.23	75.10	25.21

3.5. Solar to hydrogen efficiency:

Enhancing energy conversion efficiency stands as the ultimate objective in the endeavor to harness solar energy for photocatalytic water splitting. By assuming a catalytic reaction efficiency of 100, the upper limits of efficiency for light absorption, carrier utilization, and Solar-to-Hydrogen (STH) conversion are projected, as outlined in Table 3.

In accordance with prior studies, as outlined in Ref. [24], the efficiency of light absorption is defined as:

$$\eta_{abs} = \frac{\int_{E_g}^{\infty} P(h\omega)d(h\omega)}{\int_{0}^{\infty} P(h\omega)d(h\omega)} \quad (5)$$

In this context, $P(h\omega)$ represents the AM1.5G solar energy flux at the photon energy $h\omega$, and E_g denotes the material's band gap. The integral from E_g to ∞ in the numerator signifies the power density that materials are capable of absorbing, whereas the integral from 0 to ∞ in the denominator signifies the total power density of incident simulative sunlight (AM1.5G). Besides, the definition of carrier utilization

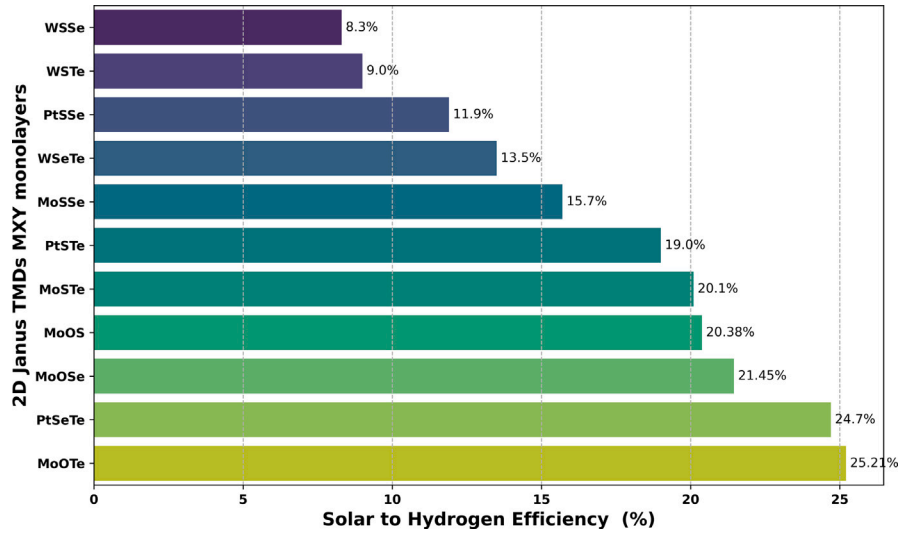

Fig. 8. The computed STH of MoOX monolayer compared with selected 2D Janus TMDs MXY monolayers.

efficiency is given by [24]:

$$\eta_{cu} = \frac{\Delta G_{H_2O} \int_E^{\infty} \frac{P(h\omega)}{h\omega} d(h\omega)}{\int_{E_g}^{\infty} P(h\omega) d(h\omega)} \tag{6}$$

In this context, ΔG_{H_2O} represents the 1.23 eV potential difference required for water splitting, and E denotes the energy of photons applicable for this process. The integral in the numerator, ranging from E to ∞, corresponds to the effective photocurrent density. It is essential to ascertain the additional energy required to surmount the barriers of HER and OER for accurately calculating Solar-to-Hydrogen (STH) efficiency. Taking into account energy losses during the migration of carriers between diverse materials, the necessary overpotentials for HER and OER are presumed to be 0.2 and 0.6 eV, respectively. Subsequently, the determination of E is achieved through [24]:

$$E = \begin{cases} E_g, (\chi(H_2) \geq 0.2, \chi(O_2) \geq 0.6) \\ E_g + 0.2 - \chi(H_2), (\chi(H_2) < 2, \chi(O_2) \geq 0.6) \\ E_g + 0.6 - \chi(O_2), (\chi(H_2) \geq 2, \chi(O_2) < 0.6) \\ E_g + 0.8 - \chi(H_2) - \chi(O_2), (\chi(H_2) < 0.2, \chi(O_2) < 0.6) \end{cases} \tag{7}$$

In that case, the definition of Solar-to-Hydrogen (STH) efficiency is as follows [24]:

$$\eta_{STH} = \eta_{abs} \times \eta_{cu} \tag{8}$$

The intrinsic Electric Field (EF) performs positive work in effecting the separation of electrons and holes during the photocatalytic water splitting process. Consequently, this specific contribution to the work must be incorporated into the overall energy calculation. Subsequently, the corrected STH efficiency for photocatalytic water splitting involving a 2D material with a vertical intrinsic EF is computed as [24]:

$$\eta'_{STH} = \eta_{STH} \times \frac{\int_0^{\infty} P(h\omega) d(h\omega)}{\int_0^{\infty} P(h\omega) d(h\omega) + \Delta\Phi \int_{E_g}^{\infty} \frac{P(h\omega)}{h\omega} d(h\omega)} \tag{9}$$

Here, $\Delta\Phi$ signifies the disparity in vacuum levels between the two surfaces of the 2D Janus MoOX materials, while the second term in the denominator encapsulates the work accomplished by the vertical inherent Electric Field (EF). The efficiency of light absorption is significantly influenced by the band gap. The band gaps of MoOS, MoOSe, and MoOTe monolayers are below 1.6 eV. Consequently, their energy conversion efficiencies for light absorption exceed 50%. Given the favorable values of $\chi(H_2)$ and $\chi(O_2)$, the energy conversion efficiencies for carrier utilization in all 2D Janus MoOX materials surpass 55%. The notable efficiencies in both light absorption and carrier utilization contribute to elevated Solar-to-Hydrogen (STH) efficiency. Due to their notably small band gaps (≤ 1.56 eV), MoOS, MoOSe, and MoOTe exhibit corrected STH efficiencies surpassing 20%. These efficiencies exceed the conventional theoretical limit of approximately 18% Table 3. In particular, MoOTe stands out with exceptional corrected Solar-to-Hydrogen (STH) conversion efficiencies of 25.21% Fig. 8. Remarkably, MoOTe is placed at the forefront among all 2D JTMDs with the general formula MXY, showcasing superior performance in the context of STH efficiency[64]. This achievement is attributed to their ability to absorb infrared light, facilitating comprehensive water splitting.

4. Conclusions

In summary, the present study employs first-principles calculations to explore the prospective implementation of the oxygenation phase of two-dimensional Janus transition metal dichalcogenides as highly efficient and eco-friendly photocatalysts for hydrogen evolution reaction. The results of our study emphasize the critical significance of the inherent electric field in shaping the functionality of the photocatalyst, given its ability to alter band alignment and surmount the limitations imposed by the band gap. Analysis of the band structure reveals semiconducting behavior, characterized by a narrow band gap ranging from 0.649 to 1.563 eV, thereby broadening light absorption across the visible and infrared spectra. The calculated solar-to-hydrogen efficiency demonstrates remarkable performance, surpassing the recognized theoretical limit. Notably, the 2D MoOTe Janus monolayer exhibits an outstanding solar-to-hydrogen efficiency of up to 25.21%, particularly under infrared light across the solar spectrum. Furthermore, meticulous analysis of Gibbs free energy differences across the studied monolayers reveals significantly reduced values during the oxygenation phase, which closely approach the optimal range compared to the parental two-dimensional Janus transition metal dichalcogenides. These findings collectively underscore the notable efficacy of the proposed materials as efficient photocatalysts for the hydrogen evolution reaction, presenting compelling opportunities for sustainable energy generation.

CRediT authorship contribution statement

Zakaryae Haman: Conceptualization, Data curation, Formal analysis, Investigation, Methodology, Software, Writing – original draft, Validation, Visualization, review & editing . **Moussa Kibbou:** Data curation, Formal analysis, Validation, Visualization, Writing – review & editing. **Nabil Khossossi:** Conceptualization, Data curation, Formal

analysis, Investigation, Methodology, Software, Validation, Visualization, Writing – review & editing. **Elhoussaine Ouabida:** Writing – review & editing. **Poulumi Dey:** Validation, Writing – review & editing. **Ismail Essaoudi:** Validation, Supervision, Writing – review & editing. **Abdelmajid Ainane:** Project administration, Resources, Supervision, Validation, Writing – review & editing.

Declaration of competing interest

The authors declare that they have no known competing financial interests or personal relationships that could have appeared to influence the work reported in this paper.

Acknowledgments

The authors gratefully acknowledge computational resources from Moulay Ismail University and Technische Universiteit Delft. A.A. acknowledges the PPR2 project:(MISTERSFC-CNRST). N.K. and P.D. acknowledge the computational resources provided by Dutch Research Organization NWO (Snellius@Surfsara) and DelftBlue supercomputer provided by Delft High-Performance Computing Centre (https://www.tudelft.nl/dhpc).

References

[1] Chen X, Li C, Grätzel M, Kostecki R, Mao SS. Nanomaterials for renewable energy production and storage. Chem Soc Rev 2012;41(23):7909–37.
[2] Kumar P, Boukherroub R, Shankar K. Sunlight-driven water-splitting using two-dimensional carbon based semiconductors. J Mater Chem A 2018;6(27):12876–931.
[3] Walter MG, Warren EL, McKone JR, Boettcher SW, Mi Q, Santori EA, et al. Solar water splitting cells. Chem Rev 2010;110(11):6446–73.
[4] Dahl S, Chorkendorff I. Towards practical implementation. Nat Mater 2012;11(2):100–1.
[5] Chen X, Shen S, Guo L, Mao SS. Semiconductor-based photocatalytic hydrogen generation. Chem Rev 2010;110(11):6503–70.
[6] Tee SY, Win KY, Teo WS, Koh L-D, Liu S, Teng CP, et al. Recent progress in energy-driven water splitting. Adv Sci 2017;4(5):1600337.
[7] Haman Z, Khossossi N, Kibbou M, Bouziani I, Singh D, Essaoudi I, et al. Computational identification of efficient 2D aluminium chalcogenides monolayers for optoelectronics and photocatalysts applications. Appl Surf Sci 2021;556:149561.
[8] Yue M, Lambert H, Pahon E, Roche R, Jemei S, Hissel D. Hydrogen energy systems: A critical review of technologies, applications, trends and challenges. Renew Sustain Energy Rev 2021;146:111180.
[9] Acar C, Dincer I. Impact assessment and efficiency evaluation of hydrogen production methods. Int J Energy Res 2015;39(13):1757–68.
[10] Zhu J, Hu L, Zhao P, Lee LYS, Wong K-Y. Recent advances in electrocatalytic hydrogen evolution using nanoparticles. Chem Rev 2019;120(2):851–918.
[11] Muradov NZ, Veziroğlu TN. "Green" path from fossil-based to hydrogen economy: an overview of carbon-neutral technologies. Int J Hydrogen Energy 2008;33(23):6804–39.
[12] Khaselev O, Bansal A, Turner J. High-efficiency integrated multijunction photovoltaic/electrolysis systems for hydrogen production. Int J Hydrogen Energy 2001;26(2):127–32.
[13] Cox CR, Lee JZ, Nocera DG, Buonassisi T. Ten-percent solar-to-fuel conversion with nonprecious materials. Proc Natl Acad Sci 2014;111(39):14057–61.
[14] Qu Y, Duan X. Progress, challenge and perspective of heterogeneous photocatalysts. Chem Soc Rev 2013;42(7):2568–80.
[15] Singh AK, Mathew K, Zhuang HL, Hennig RG. Computational screening of 2D materials for photocatalysis. J Phys Chem Lett 2015;6(6):1087–98.
[16] Fu C-F, Wu X, Yang J. Material design for photocatalytic water splitting from a theoretical perspective. Adv Mater 2018;30(48):1802106.
[17] Bolton JR, Strickler SJ, Connolly JS. Limiting and realizable efficiencies of solar photolysis of water. Nature 1985;316(6028):495–500.
[18] Jakhar M, Kumar A, Ahluwalia PK, Tankeshwar K, Pandey R. Engineering 2D materials for photocatalytic water-splitting from a theoretical perspective. Materials 2022;15(6):2221.
[19] Rosman NN, Yunus RM, Minggu LJ, Arifin K, Salehmin MNI, Mohamed MA, et al. Photocatalytic properties of two-dimensional graphene and layered transition-metal dichalcogenides based photocatalyst for photoelectrochemical hydrogen generation: An overview. Int J Hydrogen Energy 2018;43(41):18925–45.
[20] Gupta U, Rao C. Hydrogen generation by water splitting using MoS2 and other transition metal dichalcogenides. Nano Energy 2017;41:49–65.
[21] Faraji M, Yousefi M, Yousefzadeh S, Zirak M, Naseri N, Jeon TH, et al. Two-dimensional materials in semiconductor photoelectrocatalytic systems for water splitting. Energy Environ Sci 2019;12(1):59–95.
[22] Naseri M, Salahub DR, Vu TV, Zakaryae H. XSnS 3 (X=Ga, In) monolayer semiconductors as photo-catalysts for water splitting: A first principles study. J Mater Chem C 2022;10(31):11412–23.
[23] Maeda K, Domen K. Photocatalytic water splitting: Recent progress and future challenges. J Phys Chem Lett 2010;1(18):2655–61.
[24] Fu C-F, Sun J, Luo Q, Li X, Hu W, Yang J. Intrinsic electric fields in two-dimensional materials boost the solar-to-hydrogen efficiency for photocatalytic water splitting. Nano Lett 2018;18(10):6312–7.
[25] Li X, Li Z, Yang J. Proposed photosynthesis method for producing hydrogen from dissociated water molecules using incident near-infrared light. Phys Rev Lett 2014;112(1):018301.
[26] Haman Z, Khossossi N, Kibbou M, Bouziani I, Singh D, Essaoudi I, et al. Janus aluminum oxysulfide Al2OS: A promising 2D direct semiconductor photocatalyst with strong visible light harvesting. Appl Surf Sci 2022;589:152997.
[27] Liu G, Peng J, Jia B, Hao J, Zhao Z, Ma X, et al. Catalytic activity for hydrogen evolution reaction of Janus monolayer MoXTe (X=S, Se). Int J Hydrogen Energy 2023;48(37):13902–12.
[28] Ju L, Tang X, Li J, Shi L, Yuan D. Breaking the out-of-plane symmetry of Janus WSSe bilayer with chalcogen substitution for enhanced photocatalytic overall water-splitting. Appl Surf Sci 2022;574:151692.
[29] Ge D, Luo R, Wang X, Yang L, Xiong W, Wang F. Internal and external electric field tunable electronic structures for photocatalytic water splitting: Janus transition-metal chalcogenides/C3N4 van der Waals heterojunctions. Appl Surf Sci 2021;566:150639.
[30] Haman Z, Kibbou M, Khossossi N, Bahti S, Dey P, Essaoudi I, et al. Photocatalytic and thermoelectric performance of asymmetrical two-dimensional Janus aluminium chalcogenides. J Phys: Energy 2023.
[31] Jamdagni P, Kumar A, Srivastava S, Pandey R, Tankeshwar K. Photocatalytic properties of anisotropic β-PtX 2 (X=S, Se) and Janus β-PtSSe monolayers. Phys Chem Chem Phys 2022;24(36):22289–97.
[32] Chauhan P, Singh J, Kumar A. As-based ternary Janus monolayers for efficient thermoelectric and photocatalytic applications. J Mater Chem A 2023;11(19):10413–24.
[33] Zhao P, Ma Y, Lv X, Li M, Huang B, Dai Y. Two-dimensional III2-VI3 materials: Promising photocatalysts for overall water splitting under infrared light spectrum. Nano Energy 2018;51:533–8.
[34] Fan Y, Ma X, Wang J, Song X, Wang A, Liu H, et al. Highly-efficient overall water splitting in 2D Janus group-III chalcogenide multilayers: The roles of intrinsic electric filed and vacancy defects. Sci Bull 2020;65(1):27–34.
[35] Yuan J-H, Xue K-H, Miao X. Two-dimensional ABC3 (A=Sc, Y; B=Al, Ga, In; C=S, Se, Te) with intrinsic electric field for photocatalytic water splitting. Int J Hydrogen Energy 2023;48(15):5929–39.
[36] Manzeli S, Ovchinnikov D, Pasquier D, Yazyev OV, Kis A. 2D transition metal dichalcogenides. Nat Rev Mater 2017;2(8):1–15.
[37] Choi W, Choudhary N, Han GH, Park J, Akinwande D, et al. Recent development of two-dimensional transition metal dichalcogenides and their applications. Mater Today 2017;20(3):116–30.
[38] Ju L, Bie M, Tang X, Shang J, Kou L. Janus WSSe monolayer: An excellent photocatalyst for overall water splitting. ACS Appl Mater Interfaces 2020;12(26):29335–43.
[39] Haman Z, Kibbou M, Bouziani I, Benhouria Y, Essaoudi I, Ainane A, et al. Structural, electronic and optical properties of two-dimensional Janus transition metal oxides MXO (M=Ti, Hf and Zr; X=S and Se) for photovoltaic and opto-electronic applications. Physica B 2021;604:412621.
[40] Zhao T, Chen J, Wang X, Yao M. Ab-initio insights into electronic structures, optical and photocatalytic properties of Janus WXY (X/Y=O, S, Se and Te). Appl Surf Sci 2021;545:148968.
[41] Ji Y, Yang M, Lin H, Hou T, Wang L, Li Y, et al. Janus structures of transition metal dichalcogenides as the heterojunction photocatalysts for water splitting. J Phys Chem C 2018;122(5):3123–9.
[42] Kresse G, Furthmüller J. Efficiency of ab-initio total energy calculations for metals and semiconductors using a plane-wave basis set. Comput Mater Sci 1996;6(1):15–50.
[43] Kresse G, Furthmüller J. Efficient iterative schemes for ab initio total-energy calculations using a plane-wave basis set. Phys Rev B 1996;54(16):11169.
[44] Perdew JP, Burke K, Ernzerhof M. Generalized gradient approximation made simple. Phys Rev Lett 1996;77(18):3865.
[45] Heyd J, Scuseria GE, Ernzerhof M. Hybrid functionals based on a screened Coulomb potential. J Chem Phys 2003;118(18):8207–15.
[46] Blöchl PE. Projector augmented-wave method. Phys Rev B 1994;50(24):17953.
[47] Pack JD, Monkhorst HJ. "Special points for Brillouin-zone integrations"—A reply. Phys Rev B 1977;16(4):1748.
[48] Grimme S, Antony J, Ehrlich S, Krieg H. A consistent and accurate ab initio parametrization of density functional dispersion correction (DFT-D) for the 94 elements H-Pu. J Chem Phys 2010;132(15).
[49] Grimme S, Ehrlich S, Goerigk L. Effect of the damping function in dispersion corrected density functional theory. J Comput Chem 2011;32(7):1456–65.
[50] Li Y-Q, Wang X-Y, Zhu S-Y, Tang D-S, He Q-W, Wang X-C. Active asymmetric electron-transfer effect on the enhanced piezoelectricity in MoTO (T=S, Se, or Te) monolayers and bilayers. J Phys Chem Lett 2022;13(41):9654–63.

[51] Van On V, Van Ngoc H, Thuy HTP, Guerrero-Sanchez J, Hoat D. An investigation on the stability, electronic, and optical properties of new MoSO–WSO lateral heterostructures. Appl Surf Sci 2023;613:155980.
[52] Kibbou M, Haman Z, Khossossi N, Singh D, Essaoudi I, Ainane A, et al. Probing the electronic, optical and transport properties of halide double perovskites Rb2InSb (Cl, Br) 6 for solar cells and thermoelectric applications. J Solid State Chem 2022;312:123262.
[53] Kibbou M, Haman Z, Khossossi N, Essaoudi I, Ainane A, Ahuja R. Computational insights into the superior efficiency of Cs2AgGa (Cl, Br) 6 double halide perovskite solar cells. Mater Chem Phys 2023;294:126978.
[54] Kibbou M, Haman Z, Lahbi Z, Ouabida E, Essaoudi I, Ahuja R, et al. Advancing photovoltaics and optoelectronics: Exploring the superior performance of lead-free halide perovskites. Opt Mater 2024;147:114737.
[55] Kibbou M, Haman Z, Bouziani I, Khossossi N, Benhouria Y, Essaoudi I, et al. Cs2InGaX6 (X=Cl, Br, or I): Emergent inorganic halide double perovskites with enhanced optoelectronic characteristics. Curr Appl Phys 2021;21:50–7.
[56] Bouziani I, Haman Z, Kibbou M, Essaoudi I, Ainane A, Ahuja R. Electronic, optical and thermoelectric properties of two-dimensional pentagonal SiGeC4 nanosheet for photovoltaic applications: First-principles calculations. Superlattices Microstruct 2021;158:107024.
[57] Kibbou M, Haman Z, Essaoudi I, Ainane A. Designing new halide double perovskite materials Rb2AgGaX6 (X: Br, Cl) with direct band gaps and high power conversion efficiency. J Solid State Chem 2023;317:123698.
[58] Tsai C, Abild-Pedersen F, Nørskov JK. Tuning the MoS2 edge-site activity for hydrogen evolution via support interactions. Nano Lett 2014;14(3):1381–7.
[59] Nørskov JK, Bligaard T, Logadottir A, Kitchin J, Chen JG, Pandelov S, et al. Trends in the exchange current for hydrogen evolution. J Electrochem Soc 2005;152(3):J23.
[60] Greeley J, Jaramillo TF, Bonde J, Chorkendorff I, Nørskov JK. Computational high-throughput screening of electrocatalytic materials for hydrogen evolution. Nat Mater 2006;5(11):909–13.
[61] Ju L, Shang J, Tang X, Kou L. Tunable photocatalytic water splitting by the ferroelectric switch in a 2D AgBiP2Se6 monolayer. J Am Chem Soc 2019;142(3):1492–500.
[62] Zhao F, Li J, Chen Y, Zhang M, Zhang H. Photocatalytic activity of co-doped Janus monolayer MoSSe for solar water splitting: A computational investigation. Appl Surf Sci 2021;544:148741.
[63] Xia H, Shi Z, Gong C, He Y. Recent strategies for activating the basal planes of transition metal dichalcogenides towards hydrogen production. J Mater Chem A 2022;10(37):19067–89.
[64] Gao X, Shen Y, Liu J, Lv L, Zhou M, Zhou Z, et al. Boosting the photon absorption, exciton dissociation, and photocatalytic hydrogen-and oxygen-evolution reactions by built-in electric fields in Janus platinum dichalcogenides. J Mater Chem C 2021;9(42):15026–33.